AAS 13-374

REFINING SPACE OBJECT RADIATION PRESSURE MODELING WITH BIDIRECTIONAL REFLECTANCE DISTRIBUTION FUNCTIONS

Charles J. Wetterer,[*] Richard Linares,[†] John Crassidis,[‡] Tom Kelecy,[§] Marek Ziebart,[**] Moriba Jah,[††] and Paul Cefola[‡‡]

High fidelity orbit propagation requires detailed knowledge of the solar radiation pressure (SRP) on a space object. In turn, the SRP is dependent not only on the space object's shape and attitude, but also on the absorption and reflectance properties of each surface on the object. These properties are typically modeled in a simplistic fashion, but are here described by a surface bidirectional reflectance distribution function (BRDF). Several analytic BRDF models exist, and are typically complicated functions of illumination angle and material properties represented by parameters within the model. For many cases, the resulting calculation of the SRP would require a time consuming numerical integration. This might be impractical if multiple SRP calculations are required for a variety of material properties in real time, for example, in a filter where the particular surface parameters are being estimated. This paper develops a method to make accurate and precise SRP calculations quickly for some commonly used analytic BRDFs. Additionally, other non-gravitational radiation pressures exist including Earth albedo/Earth infrared radiation pressure, and thermal radiation pressure from the space object itself and are influenced by the specific BRDF. A description of these various radiation pressures and a comparison of the magnitude of the resulting accelerations at various orbital heights and the degree to which they affect the space object's orbit are also presented. Critically, this study suggests that for space debris whose interactions with electro-magnetic radiation are described accurately with a BRDF, then hitherto unknown torques would account for rotational characteristics affecting both tracking signatures and the ability to predict the orbital evolution of the objects.

[*] Principal Scientist, Pacific Defense Solutions, LLC, 1300 N. Holopono St. Suite116, Kihei, HI 96753

[†] Graduate Student, Department of Mechanical and Aerospace Engineering, University at Buffalo, Amherst, NY 14260-4400

[‡] Professor, Department of Mechanical & Aerospace Engineering, University at Buffalo, Amherst, NY 14260-4400

[§] Senior Scientist, Department 5555 Tech Center Dr. Suite 400, Colorado Springs, CO 80919

[**] Professor of Space Geodesy, Department of Civil, Environmental and Geomatic Engineering, University College London, Gower Street, London, WC1E 6BT, United Kingdom.

[††] Technical Advisor, GN&C Group, Air Force Research Laboratory, Space Vehicles Directorate, Kirtland Air Force Base, NM 87117-5776

[‡‡] Adjunct Professor, Department of Mechanical & Aerospace Engineering, University at Buffalo, Amherst, NY 14260-4400; also Consultant in Aerospace Systems, Spaceflight Mechanics, and Astrodynamics

INTRODUCTION

Observations that have been made on a special class of high area-to-mass ratio (HAMR) debris objects[1] indicate they have area-to-mass ratio (AMR) values ranging anywhere from 0.1 to 10's of m^2/kg. The resulting solar radiation pressure (SRP) perturbations, in part, explain observed variation of orbital parameters that distinguishes their long-term orbital histories. The SRP perturbation effects on orbital period, inclination and eccentricity can also produce significant variations over relatively short periods of time (days to weeks). The amplitudes and periods of the perturbations vary according to the magnitude of the AMR values[2].

Previous analyses have shown that HAMR objects have AMR values that vary with time[2-3], likely due to time varying SRP accelerations resulting from time varying solar illumination. It is hypothesized that the time varying solar illuminations are, at least in part, due to orientation changes with respect to the sun, and solar eclipsing periods. These in turn result in time varying reflective and emissive accelerations that are difficult, at best, to predict.

Work by Kelecy and Jah[4] presented a detailed SRP formulation which modeled the time varying orientation and surface thermal characteristics of HAMR objects in space, and quantified the perturbation errors due to a variety of modeling assumptions in the determination and prediction of the orbits of these objects. It was shown that the errors due to the mismodeling of thermal emissions are large enough to result in significant errors in the orbit predictions and, in particular, can result in unbalanced accelerations in directions orthogonal to the object-sun line. The analysis examined the sensitivity to the lack of *a priori* knowledge of attitude, shape or materials.

Linares et al.[5] recently demonstrated a mechanism that fuses both angles (line-of-sight) and brightness (photometric flux intensity) measurements for the purpose of orbit, attitude, and shape determination of a space object (SO). Whereas angles measurements are direct observations of the SO's orbital position, the brightness measurement is dependent on both orbital position and the SO's shape and attitude, and thus provides an indirect observation of these other attributes. The physical correlation between the SO's shape/attitude and its orbital position are caused by the various non-gravitational forces and torques, such as the SRP, which are dependent on shape and attitude, and produce a linear and angular acceleration on the SO. These non-gravitational forces and torques can become significant for HAMR objects. It has been theoretically demonstrated that simultaneously observing both angles and brightness measurements enables shape and attitude estimates that leads to improved orbit propagation. This high-fidelity orbit propagation is necessary to re-acquire the HAMR object over significant temporal sparseness in observations.

For this process to yield accurate results, however, the model used to calculate the brightness of the SO must be consistent with the model used to calculate the SRP and other non-gravitational forces and torques. Brightness models are based on the surface bidirectional reflectance distribution function (BRDF), where BRDFs define how the diffuse and specular components of light are reflected from the surface. However, SRP calculations typically use an idealized BRDF in developing the characteristic equation and, in some cases, a simplified shape model (e.g. a diffuse cannonball). In this paper, the SRP calculation is reconciled with more physically realistic BRDF functions.

The work presented here begins by establishing the dependence of the SRP on the BRDF in §2 with descriptions of various BRDFs in a common nomenclature presented in §3. The functions required to reconcile the SRP to the BRDF are then calculated in §4. Other radiation pressures, the Earth-albedo/Earth-infrared radiation pressure (ERP) and the thermal radiation pressure (TRP) are described in §5 along with how these are reconciled with the BRDF. For the TRP, this requires the development of a completely new model. Finally, the deterministic orbit and attitude propagation equations used in the analysis are described in §6 and a comparison of the magnitude of the various radiation pressures and effect on a HAMR object is presented in §7.

SRP DEPENDENCE ON BRDF

The BRDF (f_r) defines how light is reflected from an opaque surface with a given surface normal direction ($\hat{\mathbf{N}}$), illumination direction ($\hat{\mathbf{L}}$ with angles θ_i and ϕ_i from $\hat{\mathbf{N}}$), and observer direction ($\hat{\mathbf{V}}$ with angles θ_r and ϕ_r from $\hat{\mathbf{N}}$) as shown in Figure 1 and is given by

$$f_r(\theta_i,\phi_i;\theta_r,\phi_r;\lambda)=\frac{dL_r(\theta_r,\phi_r)}{dE_i(\theta_i,\phi_i)} \tag{1}$$

where dL_r is the reflected radiance in $Wm^{-2}sr^{-1}$ and dE_i is the irradiance in Wm^{-2}. The bisector vector between the illumination source and the observer is $\hat{\mathbf{H}}=(\hat{\mathbf{L}}+\hat{\mathbf{V}})/|\hat{\mathbf{L}}+\hat{\mathbf{V}}|$ with angles α and β from $\hat{\mathbf{N}}$ and is used later.

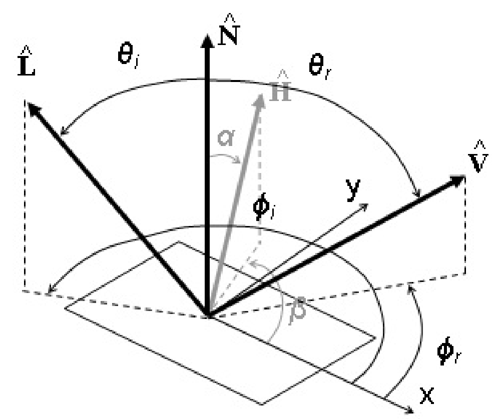

Figure 1. The Geometry of Reflection.

The acceleration caused by the SRP can be calculated by summing the individual contributions of all the constituent illuminated "facets" that make up the object, where a facet is defined as a flat surface of area A, and normal direction $\hat{\mathbf{N}}$. The acceleration is

$$\mathbf{a}_{SRP}=-\sum_{k=1}^{N_{facets}}\int_0^{\infty}\frac{F_i(\lambda)A_k f_k(\hat{\mathbf{L}}\cdot\hat{\mathbf{N}}_k)_+}{m_{SO}c}\left(\hat{\mathbf{L}}+\left(\int_{2\pi}f_r\cos\theta_r\hat{\omega}d\omega\right)_k\right)d\lambda \tag{2}$$

where $F_i(\lambda)$ is the solar flux (in $Wm^{-2}nm^{-1}$), A_k is the facet area, f_k is the fraction of the facet that is illuminated (due to self-shadowing), m_{SO} is the mass of the object, c is the speed of light, and the BRDF for each facet is integrated over all observer directions ($\hat{\omega}=\hat{\mathbf{V}}$) and all wavelengths. Additionally $(x)_+=xH(x)$ where $H(x)$ is the Heaviside step function which is one for positive values and zero for negative values. The first term in the parentheses is simply the acceleration caused by the incoming light, and the second term in the parentheses is the acceleration caused by the reflected light.

In general, the BRDF is a complicated function of illumination angle and material properties represented by parameters within the particular BRDF model. For certain BRDFs, however, the integral can be solved analytically. For example, the case of a BRDF with a Lambertian diffuse component (of diffuse reflectance ρ and fraction d) and purely "mirror-like" specular component (of specular reflectance at normal incidence F_0 and fraction $s = 1 - d$ where $\hat{\mathbf{R}}$ is the direction of mirror-like reflection)

$$f_r = d\left(\frac{\rho}{\pi}\right) + s\left(\frac{F_0 \delta\left(\hat{\omega} - \hat{\mathbf{R}}\right)}{\cos\theta_i}\right) \tag{3}$$

yields an acceleration due to the SRP of

$$\mathbf{a}_{SRP} = -\sum_{k=1}^{N_{facets}} \frac{F_{Sun} A_k f_k \left(\hat{\mathbf{L}} \cdot \hat{\mathbf{N}}_k\right)_+}{m_{SO} c} \left(\left(1 - s_k \left(F_0\right)_k\right) \hat{\mathbf{L}} + \left(\frac{2}{3} d_k \rho_k + 2 s_k \left(F_0\right)_k \hat{\mathbf{L}} \cdot \hat{\mathbf{N}}_k \right) \hat{\mathbf{N}}_k \right) \tag{4}$$

where F_{Sun} is the total solar flux over all wavelengths.

For a more complicated BRDF, the exact solution (obtained by numerically integrating Eq. (2)) is different than the idealized solution (obtained by Eq. (4)). The numerical integration of Eq. (2), however, is time consuming and might be prohibitive to calculate in certain applications. In this paper, correction factors for Eq. (4) are developed and the acceleration is calculated by using

$$\mathbf{a}_{SRP} = -\sum_{k=1}^{N_{facets}} \frac{F_{Sun} A_k f_k \left(\hat{\mathbf{L}} \cdot \hat{\mathbf{N}}_k\right)_+}{m_{SO} c} \left(\begin{array}{l} \left(1 - \left(\Delta_{s1}\right)_k s_k \left(F_0\right)_k\right) \hat{\mathbf{L}} + \\ \left(\frac{2}{3} \left(\Delta_d\right)_k d_k \rho_k + 2\left(\Delta_{s2}\right)_k s_k \left(F_0\right)_k \hat{\mathbf{L}} \cdot \hat{\mathbf{N}}_k \right) \hat{\mathbf{N}}_k \end{array} \right) \tag{5}$$

where these Δ functions are functions of the illumination angle and possibly parameters within the BRDF model. The same BRDF corrections can be applied when calculating the radiation pressure from a different illumination source, as with Earth-albedo/Earth-infrared radiation pressure (ERP), and the BRDF reflectivity differences need to be accounted for when calculating the thermal radiation pressure (TRP) due to emission from the SO itself.

BRDF DESCRIPTIONS

The reflectance models of Ashikhmin-Shirley[6,7], a simplified Blinn-Phong[8,9], and Cook-Torrance[10,11] are used in this paper. In an effort to establish a common nomenclature, the general BRDF is calculated using

$$f_r = \left(dR_d + sR_s\right) \tag{6}$$

which depends on the diffuse bidirectional reflectance (R_d) and the specular bidirectional reflectance (R_s) and the fraction of each to the total (d and s respectively where $d + s = 1$). These bidirectional reflectances are calculated differently for the various models. In each model, however, ρ is the diffuse reflectance ($0 \le \rho \le 1$) and F_0 is the specular reflectance of the surface at normal incidence ($0 \le F_0 \le 1$).

To be used as a prediction tool for brightness and radiation pressure calculations, an important aspect of the BRDF is energy conservation. For energy to be conserved, the integral of the BRDF times cos θ_r over all solid angles in the hemisphere with $\theta_r \leq 90^{\circ}$ needs to be less than unity.

$$\int_0^{2\pi}\int_0^{\pi/2} f_r \cos\theta_r \left(\sin\theta_r d\theta_r d\phi_r\right) = R_{diff} + R_{spec} \leq 1 \tag{7}$$

where R_{diff} and R_{spec} are the total diffuse and specular reflectivity respectively. For the BRDF given in Eq. (3), this corresponds to constant values of $R_{diff} = d\rho$ and $R_{spec} = sF_0$. The remaining energy not reflected by the surface is either transmitted or absorbed. In this paper it is assumed the transmitted energy is zero, and thus the emissivity of the surface can be calculated by

$$\varepsilon = 1 - \left(R_{diff} + R_{spec}\right) \tag{8}$$

The absorbed energy, thermal energy transfer between contacting surfaces, and subsequent re-emitted thermal energy is accounted for in the new TRP model developed in §5.

Ashikhmin-Shirley BRDF

Also known as the Anisotropic Phong BRDF, the diffuse and specular bidirectional reflectances are calculated using

$$R_d = \frac{28\rho}{23\pi}\left(1 - sF_0\right)\left(1 - \left(1 - \frac{\hat{\mathbf{N}}\cdot\hat{\mathbf{L}}}{2}\right)^5\right)\left(1 - \left(1 - \frac{\hat{\mathbf{N}}\cdot\hat{\mathbf{V}}}{2}\right)^5\right) \tag{9}$$

$$R_s = \frac{\sqrt{(n_u+1)(n_v+1)}}{8\pi}\frac{F}{\left(\hat{\mathbf{V}}\cdot\hat{\mathbf{H}}\right)\max\left[\hat{\mathbf{N}}\cdot\hat{\mathbf{L}}, \hat{\mathbf{N}}\cdot\hat{\mathbf{V}}\right]}\left(\cos\alpha\right)^{n_u\cos^2\beta + n_v\sin^2\beta} \tag{10}$$

where Eq. (9) is a non-Lambertian diffuse BRDF, and the Fresnel reflectance (F) in Eq. (10) is given by Schlick's approximation[7]

$$F = F_0 + \left(\frac{1}{s} - F_0\right)\left(1 - \hat{\mathbf{V}}\cdot\hat{\mathbf{H}}\right)^5 \tag{11}$$

In addition to d, ρ and F_0, the Ashikhmin-Shirley BRDF has two exponential factors (n_u, n_v) that define the anisotropic reflectance properties of each surface.

Figure 2 shows the dependence of R_{diff} and R_{spec} on illumination angle and exponential factor ($n = n_u = n_v$) for the Ashikhmin-Shirley BRDF where the integral of Eq. (7) was done numerically. In both plots, $d = s = 0.5$, and thus the simple BRDF of Eq. (3) yields $R_{diff} = R_{spec} = 0.25$ and 0.5 for the left and right plot respectively. The Ashikhmin-Shirley diffuse and specular reflectivities are not constant, however, but rather complicated functions of illumination angle, exponential factor, and the diffuse and specular reflectances. In all cases, however, $R_{diff} + R_{spec} \leq 1$, thus energy is conserved.

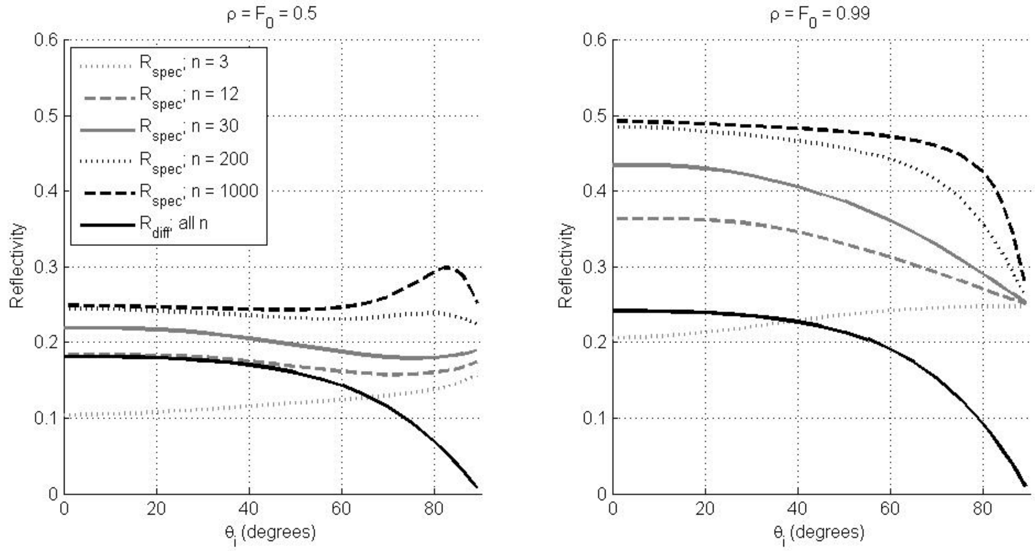

Figure 2. Ashikhmin-Shirley Diffuse and Specular Reflectivity as a Function of Illumination Angle for Various Exponential Factors.

Blinn-Phong BRDF

The specular bidirectional reflectance of the original Phong model[8] is proportional to $\left(\hat{\mathbf{N}} \cdot \hat{\mathbf{R}}\right)^n$ where $\hat{\mathbf{R}}$ is the perfect mirror-like reflection of $\hat{\mathbf{L}}$. Blinn[9] proposed that $\hat{\mathbf{H}}$ be used instead of $\hat{\mathbf{R}}$ to make it easier and faster to calculate. Unfortunately, both versions of the model do not conserve energy and thus are unsuited for the purposes of brightness estimation. The model can be made to conserve energy, however, by modifying the leading term. In keeping with the desire for simplicity in this model, the leading term is chosen to only be a function of the exponential factor and set to yield a reflectivity equal to the mirror-like reflection of Eq. (3) at normal illumination. The diffuse and specular bidirectional reflectances are thus calculated using

$$R_d = \rho/\pi \tag{12}$$

$$R_s = \frac{F_0}{8\pi} \frac{(n+2)(n+4)}{\left(n+2^{-n/2}\right)} (\cos\alpha)^n \tag{13}$$

where Eq. (12) is the Lambertian diffuse BRDF (as in Eq. (3)). In addition to d, ρ and F_0, the simplified Blinn-Phong BRDF has a single exponential factor (n) that defines the reflectance properties of each surface.

Figure 3 shows the dependence of R_{diff} and R_{spec} on illumination angle and exponential factor for the simplified Blinn-Phong BRDF where again the integral of Eq. (7) was computed numerically. The diffuse portion of the Blinn-Phong BRDF is Lambertian, and thus produces a constant diffuse reflectivity. The modification of the leading term enables energy to be conserved in all instances, but also produces the artifact of an unrealistically low specular reflectivity at grazing incident illumination.

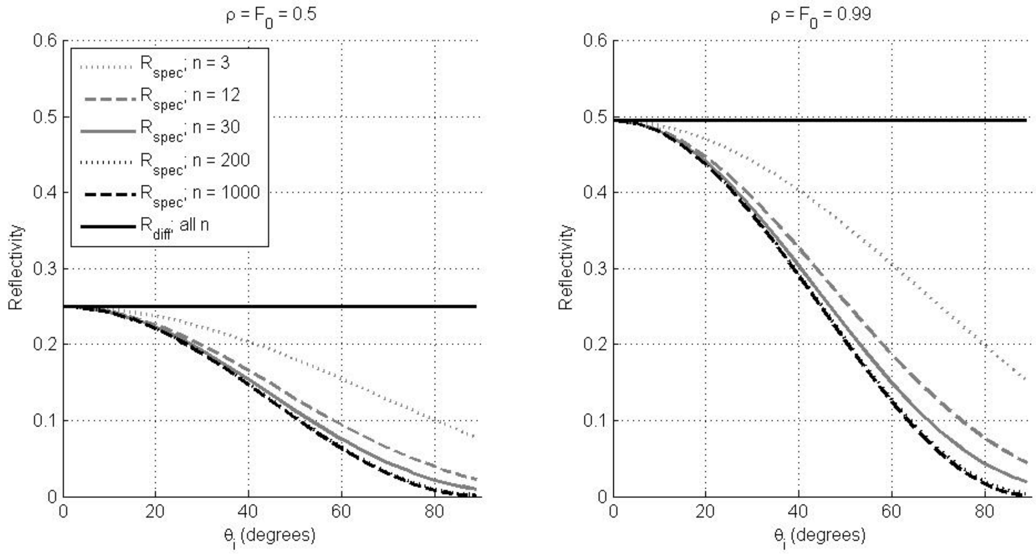

Figure 3. Blinn-Phong Diffuse and Specular Reflectivity as a Function of Illumination Angle for Various Exponential Factors.

Cook-Torrance BRDF

The diffuse and specular bidirectional reflectances are calculated using

$$R_d = \rho / \pi \tag{14}$$

$$R_s = \frac{DGF}{4(\hat{\mathbf{N}} \cdot \hat{\mathbf{L}})(\hat{\mathbf{N}} \cdot \hat{\mathbf{V}})} \tag{15}$$

where again Eq. (14) is the Lambertian diffuse BRDF (as in Eq. (3) and as with Eq. (12) for Blinn-Phong BRDF), and the facet slope distribution function (D), the geometrical attenuation factor (G) and the reflectance of a perfectly smooth surface (F) are given by

$$D = \frac{1}{\pi m^2 \cos^4 \alpha} e^{-[\tan \alpha / m]^2} \tag{16}$$

$$G = \min\left\{1, \frac{2(\hat{\mathbf{N}} \cdot \hat{\mathbf{H}})(\hat{\mathbf{N}} \cdot \hat{\mathbf{V}})}{\hat{\mathbf{V}} \cdot \hat{\mathbf{H}}}, \frac{2(\hat{\mathbf{N}} \cdot \hat{\mathbf{H}})(\hat{\mathbf{N}} \cdot \hat{\mathbf{L}})}{\hat{\mathbf{V}} \cdot \hat{\mathbf{H}}}\right\} \tag{17}$$

$$F = \frac{(g - \hat{\mathbf{V}} \cdot \hat{\mathbf{H}})^2}{2(g + \hat{\mathbf{V}} \cdot \hat{\mathbf{H}})^2}\left\{1 + \frac{[\hat{\mathbf{V}} \cdot \hat{\mathbf{H}}(g + \hat{\mathbf{V}} \cdot \hat{\mathbf{H}}) - 1]^2}{[\hat{\mathbf{V}} \cdot \hat{\mathbf{H}}(g - \hat{\mathbf{V}} \cdot \hat{\mathbf{H}}) + 1]^2}\right\} \tag{18}$$

with $g^2 = n^2 + \left(\hat{\mathbf{V}} \cdot \hat{\mathbf{H}}\right)^2 - 1$ and the index of refraction $n = \dfrac{1+\sqrt{F_0}}{1-\sqrt{F_0}}$.

In addition to d, ρ and F_0, the Cook-Torrance BRDF has a facet slope (m) parameter that defines the reflectance properties of each surface. The facet slope parameter of the Cook-Torrance BRDF and the exponential factor of the Ashikhmin-Shirley and Blinn-Phong BRDFs are roughly related by $n = 2/m^2$.

Figure 4 shows the dependence of R_{diff} and R_{spec} on illumination angle and exponential factor for the Cook-Torrance BRDF where the integral of Eq. (7) was computed numerically and $d = s = 0.5$. Again, the Lambertian diffuse portion produces a constant diffuse reflectivity, as with the Blinn-Phong BRDF. The specular portion becomes more mirror-like for smaller values of facet slope, although with significant differences in the reflectivity at high solar illumination angles. In all cases, however, energy is conserved.

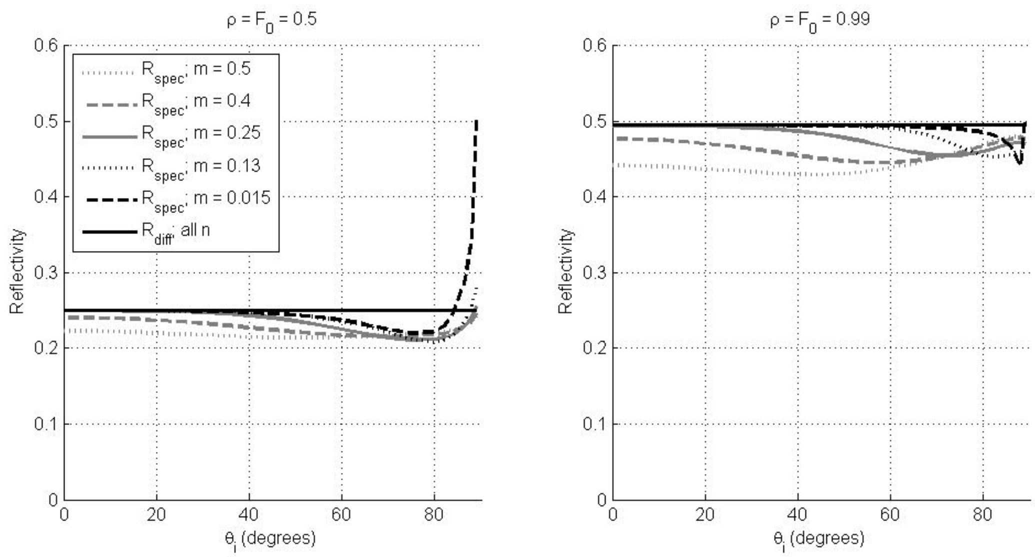

Figure 4. Cook-Torrance Diffuse and Specular Reflectivity as a Function of Illumination Angle for Various Facet Slope Values.

In general, the parameters that comprise a BRDF model can be wavelength dependent. For simplicity, this wavelength dependence is ignored and SRP correction factors for constant parameter values are derived. Adding back the wavelength dependence would simply involve adding together separate solutions weighted by the solar flux at that particular wavelength.

DERIVING THE SRP Δ FUNCTIONS

The diffuse components of the Blinn-Phong and Cook-Torrance BRDFs are Lambertian, and thus the diffuse Δ functions are simply unity. The diffuse component of the Ashikhmin-Shirley BRDF is non-Lambertian, but the integral of Eq. (2) can be evaluated analytically. The resulting diffuse Δ functions are

$$\Delta_{d-AS}(\theta_i, sF_0) = \left[\frac{31}{32}(1 - sF_0)\right]\left(\frac{1573}{1426}\right)\left(1 - \left(1 - \frac{\cos\theta_i}{2}\right)^5\right) \tag{19}$$

$$\Delta_{d-BP} = 1 \tag{20}$$

$$\Delta_{d-CT} = 1 \tag{21}$$

where the product of ρ and the term in square brackets of Eq. (19) is the equivalent Lambertian diffuse reflectance.

Values for the specular Δ's can be numerically calculated at a particular illumination angle and set of BRDF parameters by comparing Eq. (5) with the numerical integration of Eq. (2) when only considering the specular component. Specifically, for $\hat{\mathbf{L}} \neq \hat{\mathbf{N}}$,

$$\Delta_{s1}(p, \theta_i)_{numerical} = \frac{\left(\vec{\mathbf{L}}' \cdot \hat{\mathbf{N}}\right)\cos\theta_i - \left(\vec{\mathbf{L}}' \cdot \hat{\mathbf{L}}\right)}{F_0 \sin^2\theta_i} \tag{22}$$

$$\Delta_{s2}(p, \theta_i)_{numerical} = \frac{\left(\vec{\mathbf{L}}' \cdot \hat{\mathbf{N}}\right) - \left(\vec{\mathbf{L}}' \cdot \hat{\mathbf{L}}\right)\cos\theta_i}{2F_0 \cos\theta_i \sin^2\theta_i} \tag{23}$$

where p represents parameters within the BRDF model and

$$\vec{\mathbf{L}}' = \int_{2\pi} f_r\left(\hat{\omega} \cdot \hat{\mathbf{N}}, \lambda\right)\cos\theta_r \hat{\omega} d\omega \tag{24}$$

For $\hat{\mathbf{L}} = \hat{\mathbf{N}}$, the two values cannot be separated and only a composite value can be computed

$$\frac{\vec{\mathbf{L}}' \cdot \hat{\mathbf{N}}}{F_0} = -\Delta_{s1}(p, \theta_i)_{numerical} + 2\Delta_{s2}(p, \theta_i)_{numerical} \tag{25}$$

In this case, one of the specular Δ's must be estimated using nonzero illumination angles as the illumination angle approaches zero, and the other can be calculated from Eq. (25).

Once a large number of these values are obtained for a variety of input values, either an empirical fit can be made or a look-up table can be constructed. For simplicity, the anisotropy of the Ashikhmin-Shirley BRDF model is suppressed by setting the two exponential factors equal to each other ($n_u = n_v = n$). To account for the anisotropy, a more complicated correction including an azimuthal dependence would be required. The two remaining Ashikhmin-Shirley parameters that are relevant to the Δ functions are the exponential factor (n) and the multiplication of the specular fraction with the specular reflectance at normal incidence (sF_0). The exponential factor (n) is relevant for the Blinn-Phong BRDF model, while the microfacet slope (m) and the specular reflectance at normal incidence (F_0) are relevant for the Cook-Torrance BRDF model. Consequently, much of the dependence on these parameters can be eliminated by first deriving analytic solutions at special limits. Thus, the specular Δ functions are derived in three steps. In the first two steps, the BRDF in certain limits are evaluated where an analytic solution in that limit can be calculated. These correspond to the limit of normal illumination ($\hat{\mathbf{L}} = \hat{\mathbf{N}}$) and the limit when the microfacet slope parameter goes to zero (for Cook-Torrance) or the exponential factor goes to infinity (for Blinn-Phong and Ashikhmin-Shirley). The third step compares the numerical Δ values calculated for only the specular component to the analytic solution from the first two steps combined to determine the residual, and it is this residual that is turned into a look-up table.

Step 1 ($\hat{\mathbf{L}} = \hat{\mathbf{N}}$): For the case of normal illumination, each BRDF can be simplified and the integral of Eq. (2) can be accomplished analytically. The resulting Δ functions are

$$\Delta_{s1-AS} = \Delta_{s2-AS} = \Delta_{AS1}(n) = 1 - \frac{2^{3-(n+1)/2} + 8(n+1)}{(n+5)(n+3)} \tag{26}$$

$$\Delta_{s1-BP} = \Delta_{s2-BP} = \Delta_{BP1}(n) = \frac{n^2 + 2n + 8 - 4 \cdot 2^{-n/2}}{\left(n + 2^{-n/2}\right)(n+6)} \tag{27}$$

$$\begin{aligned}
&\Delta_{s1-CT} = \Delta_{s2-CT} = \Delta_{CT1}(m) = \\
&\frac{2e^{1/m^2}}{m^2}\left(Ei\left(\frac{1}{m^2}\right) + \left(4 + \frac{4}{m^2}\right)Ei\left(\frac{2}{m^2}\right) - \left(5 + \frac{4}{m^2}\right)Ei\left(\frac{4}{3m^2}\right)\right) \\
&+ \left(3 + \frac{6}{m^2}\right)e^{-1/3m^2} - \left(2 + \frac{4}{m^2}\right)e^{-1/m^2} - 1
\end{aligned} \tag{28}$$

where Ei is the exponential integral function. Due to values approaching infinity, Eq. (28) is not calculable for small values of m, and therefore an approximation must be used for $m < 0.045$ ($\Delta_{CT1}(m) = 1 - 0.0013m - 1.9634m^2$).

Step 2 ($m \to 0, n \to \infty$): Again, as the microfacet slope approaches zero or exponential factor approaches infinity, the BRDFs become more mirror-like and the integral of Eq. (2) can be accomplished. The resulting Δ functions are

$$\Delta_{s1-AS} = \Delta_{s2-AS} = \Delta_{AS2}(\theta_i, sF_0) = \frac{F(\theta_i, s, F_0)}{F_0} \tag{29}$$

$$\Delta_{s1-BP} = \Delta_{s2-BP} = \Delta_{BP2}(\theta_i) = \cos^2\theta_i \tag{30}$$

$$\Delta_{s1-CT} = \Delta_{s2-CT} = \Delta_{CT2}(\theta_i, F_0) = \frac{F(\theta_i, F_0)}{F_0} \tag{31}$$

where F in Eq. (29) is Schlick's approximation of the Fresnel reflectance from Eq. (11) with $c = \hat{\mathbf{V}} \cdot \hat{\mathbf{H}} = \cos\theta_i$ in this limit and F in Eq. (31) is the reflectance of a perfectly smooth surface defined in Eq. (18), again with $c = \hat{\mathbf{V}} \cdot \hat{\mathbf{H}} = \cos\theta_i$.

Step 3 (fitting the residual): Up to 4488 separate values for each residual were calculated corresponding to 24 different values of illumination angle (θ_i = [0°, 2°, 5°, 10°, 15°, 20°, 25°, 30°, 35°, 40°, 45°, 50°, 55°, 60°, 65°, 70°, 75°, 80°, 82° 84°, 86°, 87°, 88°, 89°]), 17 different values of microfacet slope (m = [0.005, 0.01, 0.015, 0.02, 0.04, 0.06, 0.08, 0.1, 0.13, 0.16, 0.19, 0.22, 0.25, 0.3, 0.4, 0.5, 1]) or exponential factor (n = [1, 2, 3, 5, 7, 9, 12, 15, 20, 30, 50, 100, 200, 500, 1000, 5000, 10000]), and 11 different values of specular reflectance at normal incidence (F_0 = [0.01, 0.1, 0.2, 0.3, 0.4, 0.5, 0.6, 0.7, 0.8, 0.9, 0.99]). Since the correction to the Blinn-Phong BRDF SRP is independent of F_0, only different values of illumination angle and exponential factor were evaluated.

The resulting data array was augmented into a 25 × 19 × 13 array (corresponding to $\theta_i \times n \times F_0$) for Ashikhmin-Shirley, a 25 × 19 array (corresponding to $\theta_i \times n$) for Blinn-Phong, and a 25 × 18 × 13 array (corresponding to $\theta_i \times m \times F_0$) for Cook-Torrance. Specifically, the $\theta_i = 89^o$ values were duplicated into a $\theta_i = 90^o$ matrix, an $m = 0$ or $n = 10^9$ value array was set to unity, the $n = 1$ values were duplicated into an $n = 0$ matrix, the $F_0 = 0.01$ values were duplicated into a $F_0 = 0$ matrix and the $F_0 = 0.99$ values were duplicated into a $F_0 = 1$ matrix. Values for the residual functions δ_{s1} and δ_{s2} are extracted from the data arrays via sequential linear interpolations.

The final Δ functions are thus

$$
\begin{aligned}
\Delta_{s1-AS} &= \Delta_{AS1}(n)\Delta_{AS2}(\theta_i, sF_0)\delta_{s1-AS}(\theta_i, n, F_0) \\
\Delta_{s2-AS} &= \Delta_{AS1}(n)\Delta_{AS2}(\theta_i, sF_0)\delta_{s2-AS}(\theta_i, n, F_0)
\end{aligned}
\tag{32}
$$

$$
\begin{aligned}
\Delta_{s1-BP} &= \Delta_{BP1}(n)\Delta_{BP2}(\theta_i)\delta_{s1-BP}(\theta_i, n) \\
\Delta_{s2-BP} &= \Delta_{BP1}(n)\Delta_{BP2}(\theta_i)\delta_{s2-BP}(\theta_i, n)
\end{aligned}
\tag{33}
$$

$$
\begin{aligned}
\Delta_{s1-CT} &= \Delta_{CT1}(m)\Delta_{CT2}(\theta_i, F_0)\delta_{s1-CT}(\theta_i, m, F_0) \\
\Delta_{s2-CT} &= \Delta_{CT1}(m)\Delta_{CT2}(\theta_i, F_0)\delta_{s2-CT}(\theta_i, m, F_0)
\end{aligned}
\tag{34}
$$

where $\Delta_{AS1}(n)$ is defined in Eq. (26), $\Delta_{AS2}(\theta_i, n, F_0)$ is defined in Eq. (29), $\Delta_{BP1}(n)$ is defined in Eq. (27), $\Delta_{BP2}(\theta_i)$ is defined in Eq. (30), $\Delta_{CT1}(m)$ is defined in Eq. (28), $\Delta_{CT2}(\theta_i, F_0)$ is defined in Eq. (31). The valid range for these equations are all illumination angles ($0^o \leq \theta_i \leq 90^o$), all specular reflectances at normal incidence ($0 \leq F_0 \leq 1$) and all microfacet slope values less than one ($0 \leq m \leq 1$) or exponential factors less than 10^9 ($0 \leq n \leq 10^9$).

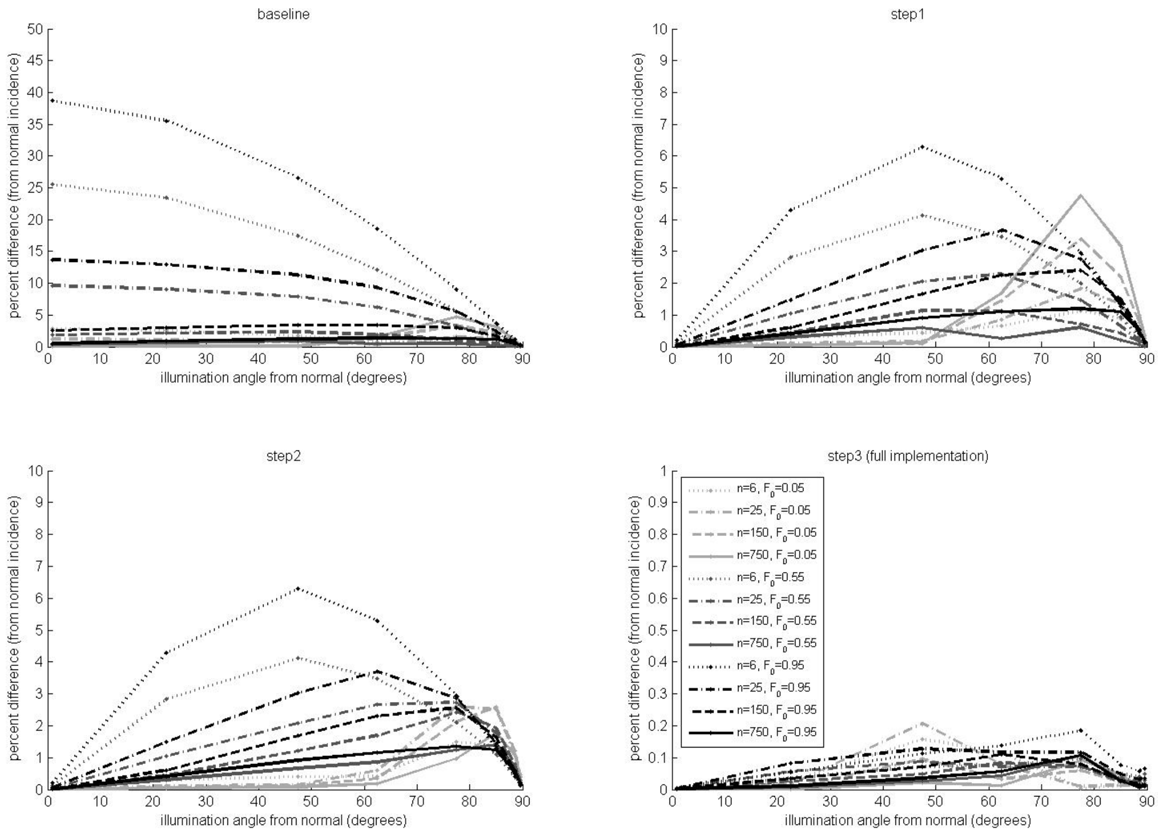

Figure 5. Percentage Difference (to acceleration at normal incidence) as a Function of Illumination Angle for Various Exponential Factors and Specular Reflectance at Normal Incidence for Ashikhmin-Shirley BRDF. No Correction (baseline), step 1, step 2, and step 3 (Full Implementation - y-axis scale 1/10th that of other plots).

Figures 5-7 show the progression from no correction through step 3 using the Δ functions described for the different BRDF models. These plots are the percentage difference with respect to the acceleration at normal incidence for values of illumination angle, microfacet slope or exponential factor, and specular reflectance at normal incidence. All values are midway between entries in the look-up tables, so represent the worst deviations that might occur. Note how in all cases, step 1 corrects the accelerations exactly for normal illumination as expected. Additionally, step 2 improves the low slope values (Cook-Torrance) and high exponential factor values (Ashikhmin-Shirley and Blinn-Phong) as expected.

The maximum uncorrected difference for Ashikhmin-Shirley is approximately 39% (for n = 6, F_0 = 0.05, and $\theta_i = 1^o$), while corrected values are <0.2%. The maximum uncorrected difference for Blinn-Phong is approximately 15% (for n = 6 and $\theta_i = 47.5^o$), while corrected values are < 0.4%. The maximum uncorrected difference for Cook-Torrance is approximately 7% (for m = 0.275, F_0 = 0.95, and $\theta_i = 1^o$), while corrected values are <0.2%.

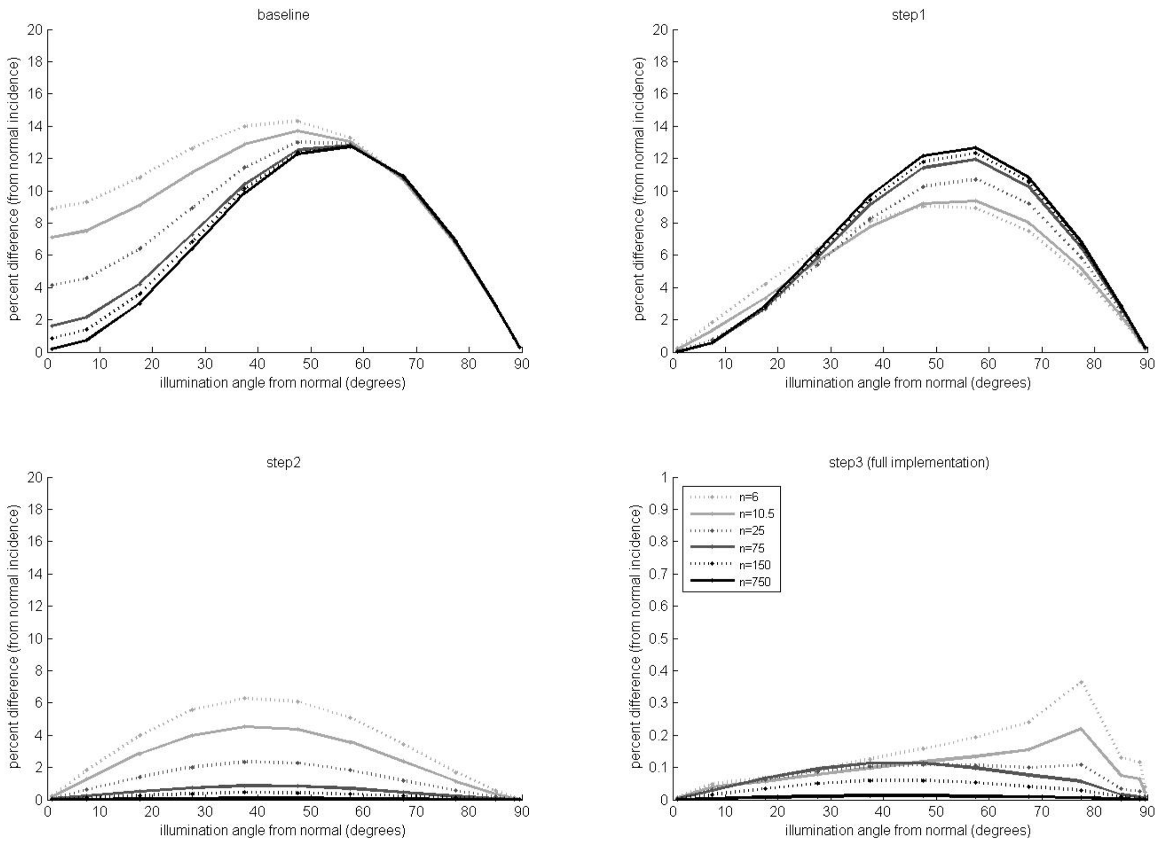

Figure 6. Percentage Difference (to acceleration at normal incidence) as a Function of Illumination Angle for Various Exponential Factors and Specular Reflectance at Normal Incidence for Blinn-Phong BRDF. No Correction (baseline), step 1, step 2, and step 3 (Full Implementation - y-axis scale 1/10th that of other plots).

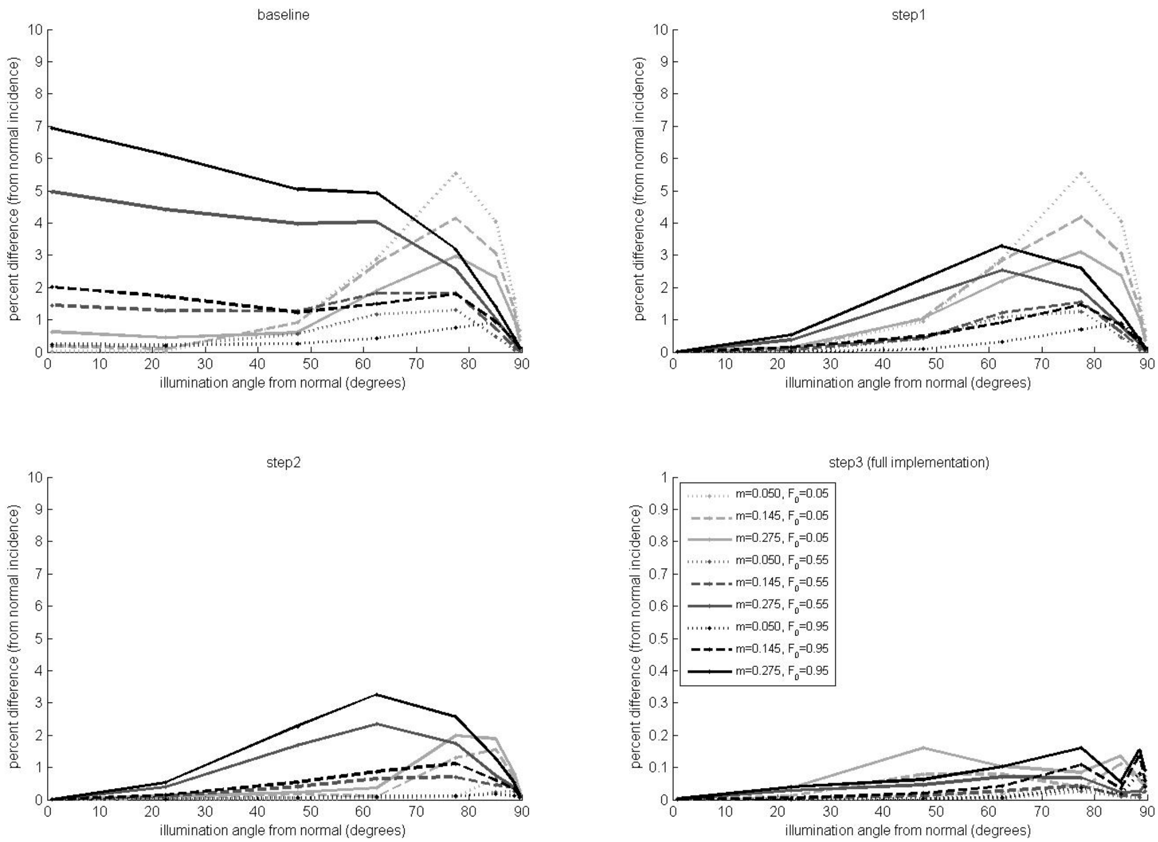

Figure 7. Percentage Difference (to acceleration at normal incidence) as a Function of Illumination Angle for Various Microfacet Slopes and Specular Reflectance at Normal Incidence for Cook-Torrance BRDF. No Correction (baseline), step 1, step 2, and step 3 (Full Implementation - y-axis scale 1/10th that of other plots).

OTHER RADIATION PRESSURE MODELS

Other sources of radiation pressure exist where the difference from the baseline of Eq. (4) are comparable to the BRDF SRP correction of Eq. (5). Earth-albedo and Earth-infrared radiation pressure (ERP) is identical in form to the SRP where the Earth's reflection in the visible and emission in the infrared takes the place of the Sun as the illumination source. Calculation of the ERP acceleration is more complicated due to the larger solid angle subtended by the Earth with respect to the SO and the introduction of an empirical model to represent the Earth's albedo and emissivity. As with the SRP acceleration, the SO's surface BRDF also needs to be considered. The final radiation pressure to be considered is the SO's thermal radiation pressure (TRP). To calculate the TRP acceleration, one must know the temperatures of the various surfaces of the SO. This requires a model that calculates these temperatures given the SO's attitude, the passage of each surface into and out of shadow, and the thermal interconnection between surfaces.

Earth-Albedo/Earth-Infrared Radiation Pressure

A slightly modified model of Knocke et al.[12,13] is used to calculate the ERP acceleration. In this model, the Earth is divided into N regions and Eq. (4) is used to calculate the contribution of each region to the space object's acceleration by using

$$\mathbf{a}_{ERP} = -\sum_{k=1}^{N_{facets}} \sum_{j=1}^{N} \frac{F_{Earth,j} A_k f_k \left(\hat{\mathbf{L}}_j \cdot \hat{\mathbf{N}}_k\right)_+}{m_{SO} c} \left(\begin{array}{l} \left(1 - s_k (F_0)_k\right) \hat{\mathbf{L}}_j \\ + \left(\frac{2}{3} d_k \rho_k + 2 s_k (F_0)_k \hat{\mathbf{L}}_j \cdot \hat{\mathbf{N}}_k \right) \hat{\mathbf{N}}_k \end{array} \right) \tag{35}$$

The total Earth flux for each region j is calculated by

$$F_{Earth,j} = F_{Sun} \left(a_j \left(\cos\theta_j\right)_+ + \frac{1}{4}\varepsilon_j \right) \frac{4\pi R_\oplus^2}{N} \frac{\left(\cos\alpha_j\right)_+}{\pi r_j^2} \tag{36}$$

where F_{Sun} is the total solar flux as used in Eqs. (3 - 5), a_j is the Earth's albedo, θ_j is the angle between the solar illumination vector and normal to the surface of the j^{th} Earth region, ε_j is the Earth's emissivity, α_j is the angle between the viewing vector (center of j^{th} Earth region to SO) and normal to the surface of the Earth region, and r_j is the distance from the center of j^{th} Earth region to the SO. Knocke et al. used N = 19 regions consisting of a single sub-object region and 6 and 12 regions in two concentric rings, all with equal projected and attenuated areas. Instead, as reflected in Eq. (35), in this paper the entire Earth surface is divided into N evenly distributed and equal area regions and ERP accelerations are calculated from only those regions visible from the space object ($\cos \alpha > 0$). N is chosen based on the SO's altitude to ensure at least 40 regions are visible at any one time.

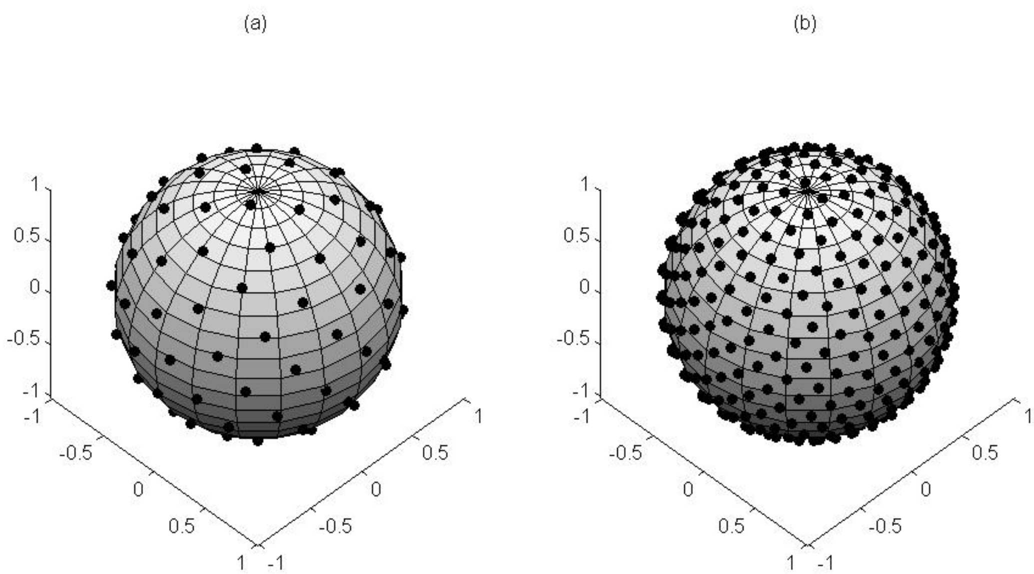

Figure 8. (a) N = 100 and (b) N = 400 Distribution of Earth Regions on Unit Sphere.

The process used to generate the N evenly distributed regions employs a slight variation to the prescription of Rakhmanov et al.[14,15] Specifically, the region centers (latitude and longitude in radians) are calculated using

$$\lambda_j = \tan^{-1}\left(\frac{\sqrt{1-z_j^2}}{z_j}\right) - \frac{\pi}{2} \tag{37}$$

$$l_j = \operatorname{mod}\left(l_{j-1} + \pi\left(3-\sqrt{5}\right), 2\pi\right) \tag{38}$$

for $j = 1 \ldots N$, where $z_1 = 1 - 1/N$, $l_1 = 0$, and $z_j = z_{j-1} - 2/N$. Figure 8 displays this distribution for $N = 100$ and $N = 400$ for (a) and (b) respectively.

The Earth's albedo and emissivity are empirical functions of latitude and also account for seasonal variations:

$$a = a_0 + a_1 P_1(\sin\lambda) + a_2 P_2(\sin\lambda) \tag{39}$$

$$\varepsilon = \varepsilon_0 + \varepsilon_1 P_1(\sin\lambda) + \varepsilon_2 P_2(\sin\lambda) \tag{40}$$

where $a_0 = 0.34$, $a_1 = 0.1\cos(2\pi(JD - t_0)/365.25)$, $a_2 = 0.29$, $\varepsilon_0 = 0.68$, $\varepsilon_1 = -0.07\cos(2\pi(JD - t_0)/365.25)$, $\varepsilon_2 = -0.18$. JD is the Julian Date, $t_0 = 2444960.5$ (1981 Dec 22), λ is the Earth region's latitude, and P_1 and P_2 are Legendre polynomials of orders 1 and 2 respectively. Although computationally expensive, the equivalent to Eq. (5) can be easily used to calculate the BRDF corrected ERP.

Thermal Radiation Pressure

A new thermal model is developed that is compatible with the surface BRDF. First, however, the thermal model of Marshall and Luthke[16] is examined to provide a comparison in calculating the TRP. In this model, as with the SRP and ERP, the contribution of each facet is calculated separately and then summed. The acceleration is

$$\mathbf{a}_{TRP} = -\sum_{k=1}^{N_{facets}} \frac{2\varepsilon_k \sigma T_k^4 A_k}{3 m_{SO} c} \hat{\mathbf{N}}_k \tag{41}$$

where ε_k is the emissivity of the particular surface, σ is the Stefan-Boltzmann constant, and T_k is the temperature of the particular surface. This equation assumes the emissivity is independent of emission angle (i.e. it can be represented by a Lambertian-like function). The temperatures are determined using empirical functions of the form

$$T = k_1 + k_2 \cos\left(\frac{\theta_i}{k_3}\right)\left[1 - \exp\left(\frac{-(t_1 + s_1)}{k_4}\right)\right] \tag{42}$$

where

$$s_1 = -k_4 \ln\left(\max\left[1 - \exp\left(\frac{-t_2}{k_5} \right) \frac{\cos\theta_{shadow}}{\cos\theta_{sun}}, 0.0001 \right] \right) \tag{43}$$

for illuminated surfaces, and

$$T = k_1 + k_2 \exp\left(\frac{-(t_2 + s_2)}{k_5} \right) \tag{44}$$

where

$$s_2 = -k_5 \ln\left(\max\left[\cos\left(\frac{\theta_{shadow}}{k_3} \right), 0.0001 \right] \right) \tag{45}$$

for surfaces in shadow where the temperature cools to some specified minimum in a time dependent on the material characteristics. The adjustable material parameters for each surface are k_1 (cold equilibrium temperature), k_2 (difference between cold and hot equilibrium temperatures), k_3 (rotational rate/thermal inertia constant), k_4 (transition time from hot to cold equilibrium temperature), and k_5 (transition time from cold to hot equilibrium temperature). The other quantities are values that need to be calculated for a particular surface: t_1 (time since shadow exit), t_2 (time since shadow entry), θ_i (illumination angle), θ_{shadow} (illumination angle at shadow entry), and θ_{sun} (illumination angle at shadow exit).

Implicit in this model is the emissivity as related to the diffuse and specular reflectances. For the simple Lambertian diffuse and mirror-like specular BRDF, to conserve energy, this reduces to

$$\varepsilon = 1 - R_{diff} - R_{spec} = 1 - d\rho - sF_0 \tag{46}$$

Empirical values for various surfaces typical of spacecraft materials are shown in columns 1-8 in Table 1 (from Table 5 in Ref 15). The values to be modeled in this simulation are shown in column 9.

Table 1. Sample TRP Model Values

	1	2	3	4	5	6	7	8	9
k_1 (K)	181	168	191	190	240	103	236	234	250
k_2 (K)	233	178	18	63	98.5	125	110	96	50
k_3	1.25	1.00	1.05	1.00	1.06	1.15	1.00	1.00	1.25
k_4 (s)	621	282	759	426	519	680	805	806	700
k_5 (s)	111	120	624	487	767	413	828	866	500

The key to calculating the TRP is determining the temperatures of each surface of the SO. The temperature of a surface depends on three quantities: heating of the surface due to radiation (e.g. solar or Earthshine), cooling of the surface due to radiation (e.g. blackbody emission that produces the TRP), and heating/cooling of the surface due to conduction (e.g. connection to other surfaces or components of the SO). From one time step to the next, this can be summarized in the equation

$$(T_{i+1})_k = (T_i)_k + \frac{(P_{absorb} + P_{emit} + P_{conduct})_k \Delta t}{C_k} \tag{47}$$

where C is the heat capacity related to the surface (in Joules per Kelvin). The power being absorbed by the surface can be represented by

$$(P_{absorb})_k = \sum_{j=1}^{N_{sources}} \left(1 - (R_{diff})_{j,k} - (R_{spec})_{j,k}\right) F_j A_k \left(\hat{\mathbf{L}}_j \cdot \hat{\mathbf{N}}_k\right)_+ \tag{48}$$

where A is the surface area, $\hat{\mathbf{L}}_j$ is the direction to the illumination source, and $\hat{\mathbf{N}}$ is the surface normal, R_{diff} and R_{spec} are the diffuse and specular reflectivity of the k^{th} facet for the j^{th} illumination source, and F_j is the total flux over all wavelengths of an illumination source (e.g. Sun or Earth region). Note that P_{absorb} is always positive. The power being emitted from the surface can be represented by

$$(P_{emit})_k = -\varepsilon_k A_k \sigma T_k^4 \tag{49}$$

which is simply the blackbody radiation at a particular temperature. The emissivity of the k^{th} facet to be used in Eqs. (49) and (41), to be consistent with the surface BRDF, is calculated using

$$\varepsilon_k = 1 - \left(R_{diff} + R_{spec}\right)_{\hat{L}=\hat{N}} \tag{50}$$

where the $\hat{\mathbf{L}} = \hat{\mathbf{N}}$ notation in the subscript signifies these are the diffuse and specular reflectivity associated with that geometry for the given BRDF parameters. Note that P_{emit} is always negative. Finally, the power being conducted to or from the surface can be represented by

$$(P_{conduct})_k = \sum_{kk=1}^{N_{body}} A_{kk,k} k_{kk,k} \left(\vec{\nabla} T\right)_{kk,k} \tag{51}$$

where k, A and $\left(\vec{\nabla} T\right)$ are the various conductivities, contact surface areas, and temperature gradients between the the k^{th} surface and the N_{body} other portions of the object. $P_{conduct}$ is positive when energy flows into the surface and negative when energy flows out of the surface.

The additional parameters required for each surface in this model beyond those associated with the BRDF is a term related to the surface heat capacity (in Eq. (47)) and terms related to the conductivities and contact surface areas between the surface and other parts of the object (in Eq. (51)). In practice, the assumption that Eq. (51) and the associated parameters can be replaced by two parameters is made such that

$$(P_{conduct})_k = -K_k \left(T_k - T_{body}\right) \tag{52}$$

where K is a term related to conductivity of each surface (in Watts per Kelvin) and T_{body} is an equilibrium temperature for the body as a whole. Thus, for a cube, this TRP model would require 13 total parameters to represent the SO as opposed to 30 total parameters in the Marshall-Luthke model. When all the surfaces are identical, 3 total parameters would be necessary as opposed to 5 total parameters in the Marshall-Luthke model.

The temperatures of all six sides of a slowly rotating cube fixed in space with the Sun as the only illumination source as predicted by the Marshall-Luthke model using the values in column 9 of Table 1 are calculated and displayed in Figure 9. The cube is rotating at 0.017 rad/s about it's *z*-axis. The slight discontinuity on the declining slope of the ±x and ±y temperature curves corresponds to the time when the side goes into shadow due to the rotation of the cube and the temperature changes from being calculated with Eqs. (42) and (43) to Eqs. (44) and (45).

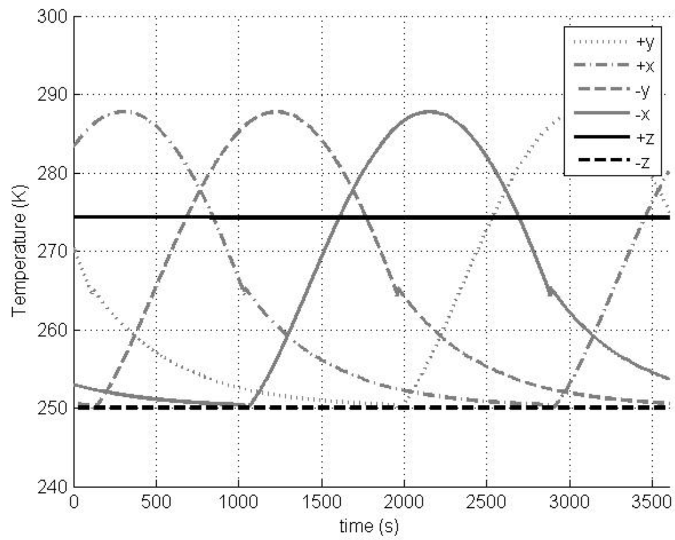

Figure 9. Temperatures of the Different Sides of a Slowly Rotating Cube with Identical Marshall-Luthke Surface Parameters.

The –*z*-axis of the cube is facing away from the Sun, so is at the constant cold temperature of k_1 = 250 K, while the +*z*-axis of the cube is illuminated by the Sun at a constant non-normal angle, so is at a constant temperature less than $k_1 + k_2$ = 300 K. The other sides alternatively are illuminated by the Sun and then are in shadow, and since they are identical, they exhibit the same temperature profile as a function of time.

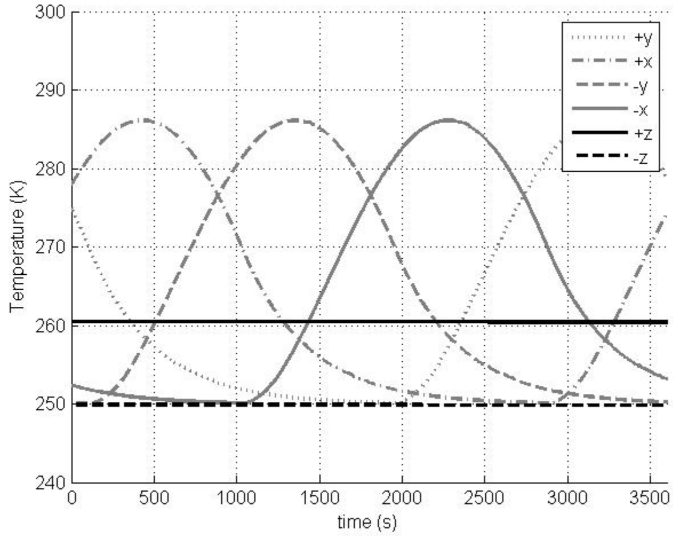

Figure 10. Temperatures of the Different Sides of a Slowly Rotating Cube with Identical Surface Parameters of New TRP Model.

Figure 10 displays the temperatures of all six sides of the same cube using the new TRP BRDF corrected model with C = 9000 J/K, K = 20 W/K, and T_{body} = 258 K, and the Ashikhmin-Shirley BRDF with $\rho = F_0 = 0.5$, $d = s = 0.5$, and $n_u = n_v = 10$. The TRP model values were determined by trial and error to produce temperature profiles similar to those in Figure 9. In general, adjusting C alters the rate at which the surface heats and cools, with a greater value of C resulting in a longer heating/cooling time, adjusting K alters the peak temperature, with a greater value of K resulting in a lower peak temperature, and adjusting T_{body} alters the overall level of the temperature profile.

There are some features between the models that are not reconciled. Most notable is the +z-axis facing side's temperature. In both models it is constant due to the constant solar illumination. The level in the Marshall-Luthke model, however, is significantly higher than the new model. The other significant difference is the timing of the peak temperature on the x-axis and y-axis sides with the Marshall-Luthke model peaking earlier than the new model. Likely the new model is unable to replicate exactly the temperature profiles of the Marshall-Luthke model. The new model, however, has the advantage of being physics based and reconciled with the surface BRDF, and so is used in the remainder of the paper.

ORBIT AND ATTITUDE PROPAGATION

The principal purpose of the trajectory and attitude modeling carried out in this paper is to emphasize the difference in behavior of the SO predicted by conventional surface force models with that predicted by BRDF-corrected techniques. Hence the conservative force field is treated simplistically whereas the surface forces are given a rigorous formulation.

In this paper the position and velocity of an Earth orbiting SO are denoted by $\mathbf{r}^I = [x, y, z]^T$ and $\mathbf{v}^I = [v_x, v_y, v_z]^T$, respectively. The Newtonian two-body gravitational equations of motion with radiation pressure acceleration in Earth-centered inertial coordinates (ECI) are given by

$$\ddot{\mathbf{r}}^I = -\frac{\mu}{\left\|\vec{r}^I\right\|^3}\mathbf{r}^I + \mathbf{a}_{total}^I + \mathbf{a}_{J2}^I \tag{53}$$

where the terms μ represents the gravitational parameter of the Earth and $\mathbf{a}_{total}^I = \sum_{k=1}^{N_{sides}} \mathbf{a}_k^I$ represents the acceleration perturbation due the various radiation pressures as described previously and summed over all the surfaces, while $\mathbf{a}_{J2}^I$ is the gravitational perturbation due to non-symmetric distribution of mass along the lines of latitude of the Earth. The acceleration due to the J2 effect is given by[17]

$$\mathbf{a}_{J2}^I = -\frac{3}{2}J_2\left(\frac{\mu}{\left\|\vec{r}^I\right\|}\right)\left(\frac{R_\oplus}{\left\|\vec{r}^I\right\|}\right)^2\begin{bmatrix}\left(1-5\left(\frac{z}{\left\|\vec{r}^I\right\|}\right)^2\right)\frac{x}{\left\|\vec{r}^I\right\|}\\ \left(1-5\left(\frac{z}{\left\|\vec{r}^I\right\|}\right)^2\right)\frac{y}{\left\|\vec{r}^I\right\|}\\ \left(3-5\left(\frac{z}{\left\|\vec{r}^I\right\|}\right)^2\right)\frac{z}{\left\|\vec{r}^I\right\|}\end{bmatrix} \tag{54}$$

where $J_2 = 1.082\ 626\ 683\times10^{-3}$ is the coefficient for the second zonal harmonic and $R_\oplus =$ 6,378.137 km is the mean equatorial radius of the Earth.

A number of parameterizations exist to specify attitude, including Euler angles, quaternions, and Rodrigues parameters[18]. This paper uses the quaternion, which is based on the Euler angle/axis parameterization. The quaternion is defined as $\mathbf{q} = \begin{bmatrix}\boldsymbol{\xi}^T & q_4\end{bmatrix}^T$ with $\boldsymbol{\xi} = \begin{bmatrix}q_1 & q_2 & q_3\end{bmatrix}^T = \hat{\mathbf{e}}\sin(\upsilon/2)$ and $q_4 = \cos(\upsilon/2)$, where $\hat{\mathbf{e}}$ and υ are the Euler axis of rotation and rotation angle, respectively. This vector must satisfy the constraint $\mathbf{q}^T\mathbf{q} = 1$. The attitude matrix can be written as a function of the quaternion by

$$A = \Xi(\mathbf{q})^T\Psi(\mathbf{q}) \tag{55}$$

where

$$\Xi(\mathbf{q}) = \begin{bmatrix} q_4 I_{3\times3} + [\boldsymbol{\xi}\times] \\ -\boldsymbol{\xi}^T \end{bmatrix} \tag{56}$$

$$\Psi(\mathbf{q}) = \begin{bmatrix} q_4 I_{3\times3} - [\boldsymbol{\xi}\times] \\ -\boldsymbol{\xi}^T \end{bmatrix} \tag{57}$$

and

$$
[\mathbf{a}\times] = \begin{bmatrix} 0 & -a_3 & a_2 \\ a_3 & 0 & -a_1 \\ -a_2 & a_1 & 0 \end{bmatrix} \tag{58}
$$

for any general 3×1 vector $\mathbf{a}$. The quaternion kinematics equation is given by

$$
\dot{\mathbf{q}} = \frac{1}{2}\Xi(\mathbf{q})\boldsymbol{\omega} \tag{59}
$$

where $\boldsymbol{\omega}$ is the angular velocity. The angular velocity dynamic equation can be written as

$$
\dot{\boldsymbol{\omega}} = \bar{\bar{J}}^{-1}\left(\mathbf{M} - [\boldsymbol{\omega}\times]\bar{\bar{J}}\boldsymbol{\omega}\right) \tag{60}
$$

where $\bar{\bar{J}}$ the inertia tensor for the SO and $\mathbf{M}$ are any external applied torques. The SO is assumed to be a rectangular prism (sides *a* and *b* and length *l*) therefore the principle components of the inertia tensor are given by simple equations:

$$
J_1 = m_{SO}\frac{\left(a^2+b^2\right)}{12} \quad J_2 = m_{SO}\frac{\left(a^2+l^2\right)}{12} \quad J_3 = m_{SO}\frac{\left(l^2+b^2\right)}{12} \tag{61}
$$

The radiation pressure moments can be calculated by considering that the forces act through the center of each facet. Then the radiation pressure moment can be written as

$$
\mathbf{M} = m_{SO}\sum_{k=1}^{N_{sides}}\left[\mathbf{r}_k^B\times\right]A(\mathbf{q})\mathbf{a}_k^I \tag{62}
$$

where $\mathbf{r}_k^B$ is the location of the geometric center of each facet with respect to the center of mass of the SO in body coordinates and $A(\mathbf{q})$ is the attitude matrix calculated by the quaternion $\mathbf{q}$. The radiation pressure moment is used with Eq. (60) to simulate the rotational dynamics of the SO.

RADIATION PRESSURE PERTURBATION COMPARISONS

A 1-m cube HAMR object that is 1-kg in mass is placed in GEO, a GPS orbit, and a 1000-km height Sun-synchronous LEO, with Table 2 listing the orbital details.

Table 2. Orbit Specifications

	GEO	GPS	LEO
a (km)	42164	26560	7378
ε	0	0	0
i (deg)	0	55	98
M_0 (deg)	90	90	90
ω (deg)	0	0	0
Ω (deg)	0	0	0

The SRP in Eq. (2), BRDF-corrected SRP using the Ashikhmin-Shirley BRDF with $n_u = n_v$ = 10 in Eq. (10), ERP in Eq. (35) and TRP with C = 9000 J/K, K = 20 W/K, and T_{body} = 258 K in Eq. (41) are calculated and compared as well as the differences in total, radial, in-track, and cross-track distances as a function of time. Each surface of the cube is identical with $\rho = F_0 = 0.5$, $d = s = 0.5$, and $\varepsilon = 0.5$.

In this simulation, the initial attitude, using the quaternion parameterization, is set to $\mathbf{q} = [0.7041; 0.199; 0.0896; 0.7041]^T$, the initial angular rate is zero, and the values are propagated for 7 days with a 6 s time step. The initial date and time are 2010 Mar 15, UT 4:00:00. It should be noted that these tests are designed to highlight the differing trajectory and attitude behaviors predicted by the various radiation pressures (SRP vs. ERP vs. TRP) and the two modeling approaches (traditional SRP vs. BRDF-corrected SRP).

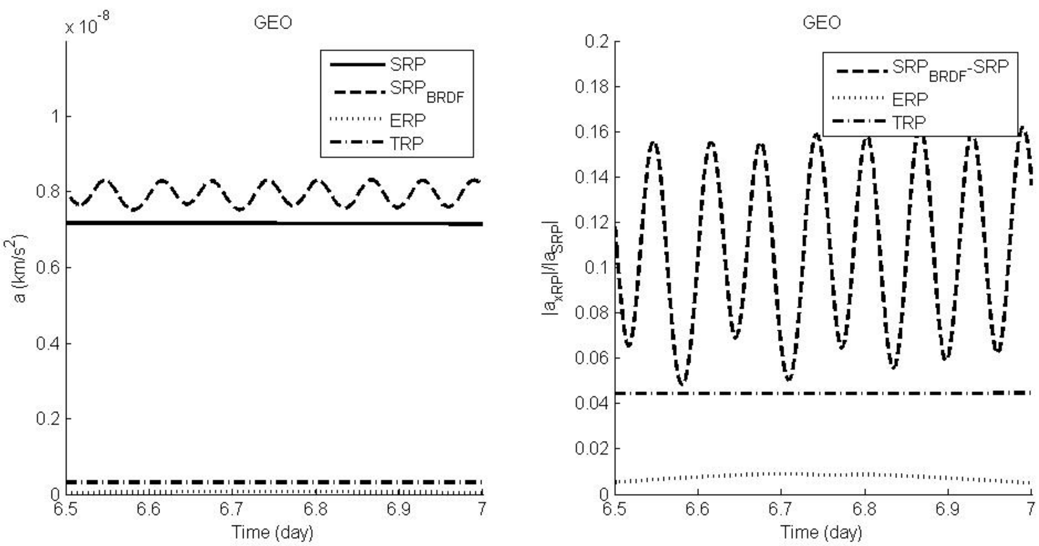

Figure 11. (a) Absolute Magnitude of Radiation Force, and (b) Fractional Difference for Out of Eclipse Times for GEO.

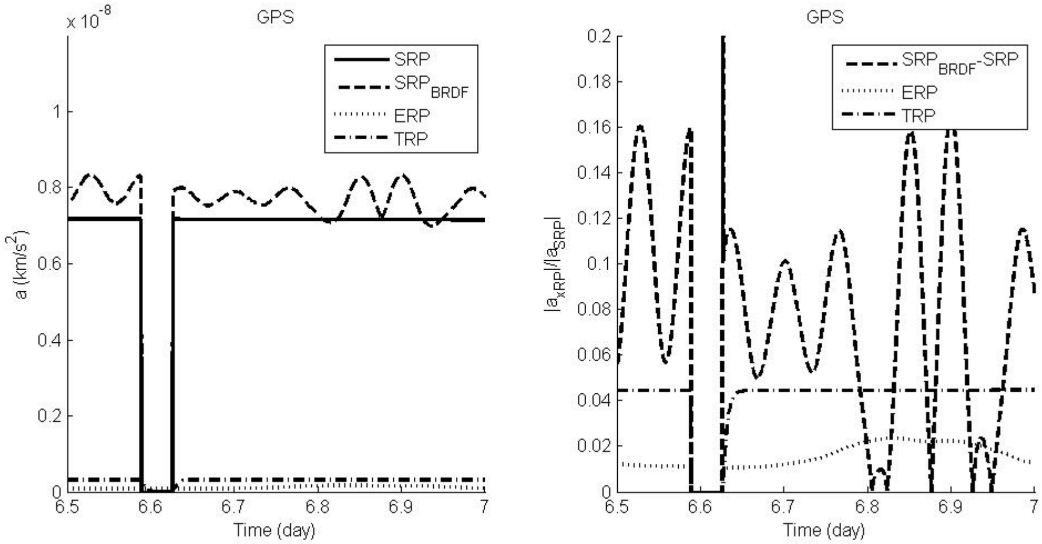

Figure 12. (a) Absolute Magnitude of Radiation Force, and (b) Fractional Difference for Out of Eclipse Times s for GPS orbit.

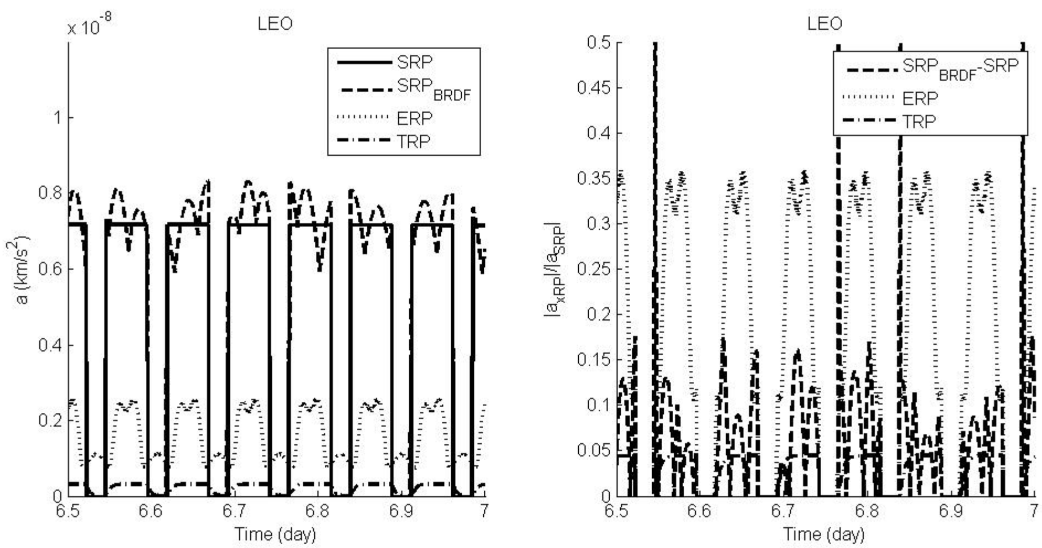

Figure 13. (a) Absolute Magnitude of Radiation Force, and (b) Fractional Difference for Out of Eclipse Times for LEO.

Figures 11-13 plot the absolute magnitude of the various radiation forces as a function of time for the HAMR object at GEO, a GPS orbit, and LEO, respectively, for the last half day of the simulation. Also plotted are the fractional differences of the BRDF-corrected SRP to the SRP and the relative difference of the ERP and TRP to the SRP for times when the object is out of eclipse. Whereas the relative magnitude of the TRP and difference of the BRDF-corrected SRP to the SRP remains about the same for each orbit type, the magnitude of the ERP depends on radial distance as expected. Note the regular entry into and exit out of earth eclipse in the acceleration time histories coincident with the orbit of the satellite.

Of particular note is the variation in magnitude of the BRDF-corrected SRP to the others. This results from the fact that only the BRDF-corrected SRP produces a torque on the HAMR object resulting in attitude changes and thus variations in the projected area and resulting acceleration. For a rectangular prism, the SRP and ERP (with the simple Lambertian diffuse and mirror-like specular BRDF) and TRP (with the Lambertian emissivity) do not produce a torque. The BRDF-corrected SRP, however, does produce a torque because the specular reflectivity is a function of the illumination angle and the specular reflection is not exactly at the angle of the mirror-like reflection.

Figures 2-4 illustrated the former point while Figure 14 illustrates the latter point by plotting the difference between the actual angles of peak specular reflection to the mirror like angle as a function of illumination angle for various values of the exponential factor in the Ashikhmin-Shirley BRDF. As expected, as the exponential factor increases, the specular reflection becomes more and more mirror-like.

This significant difference between the rotational dynamics of the SO when using the simplistic SRP of Eq. 4 and the BRDF-corrected SRP of Eq. 5, highlighted by the discovery of a hitherto unknown torque caused by the specular reflectance of the SO's surface, illustrates the importance of accounting for these effects.

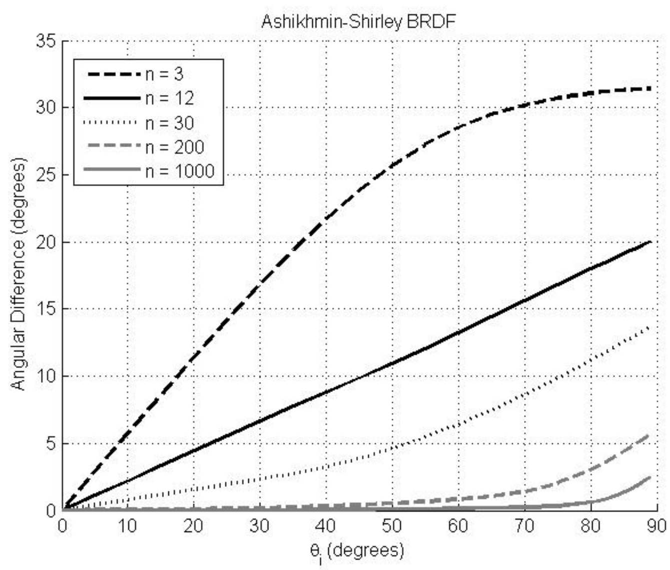

Figure 14. Difference Between Actual Angles of Peak Specular Reflection to the Mirror-Like Angle as a Function of Illumination Angle.

Figures 15-17 plot the total difference, radial difference, in-track difference, and cross-track difference for positions calculated using the SRP, BRDF-corrected SRP, SRP + ERP, and SRP + TRP as compared to the position with the SRP on a completely absorptive cannonball (SRP-AC) of 1.2 m^2 cross-sectional area as a function of time for the last half day of the simulation. For the most part, to this scale, the differences are all very similar.

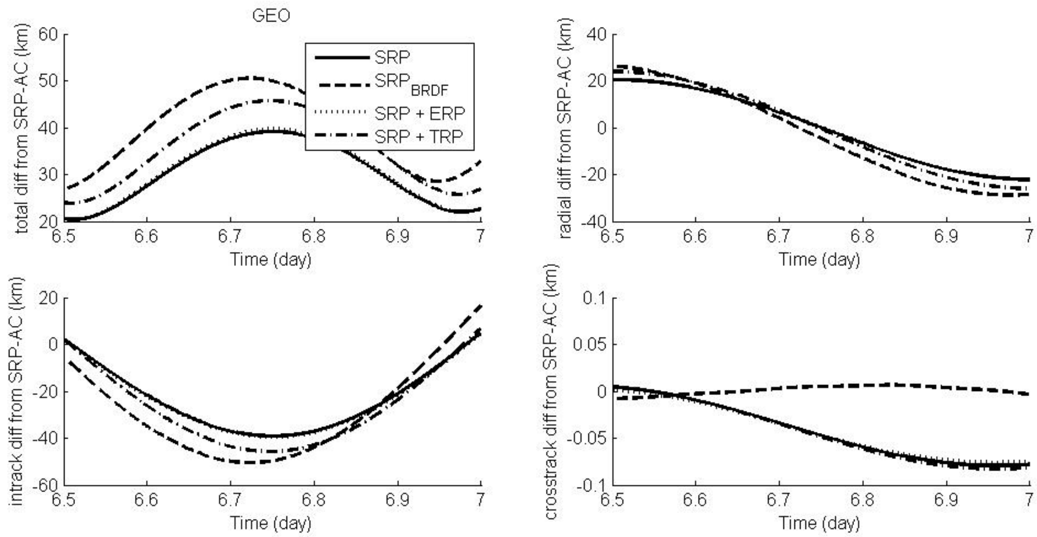

Figure 15. (a) Total Difference, (b) Radial Difference, (c) In-Track Difference, and (d) Cross-Track Difference in Positions from SRP on completely absorptive cannonball for GEO.

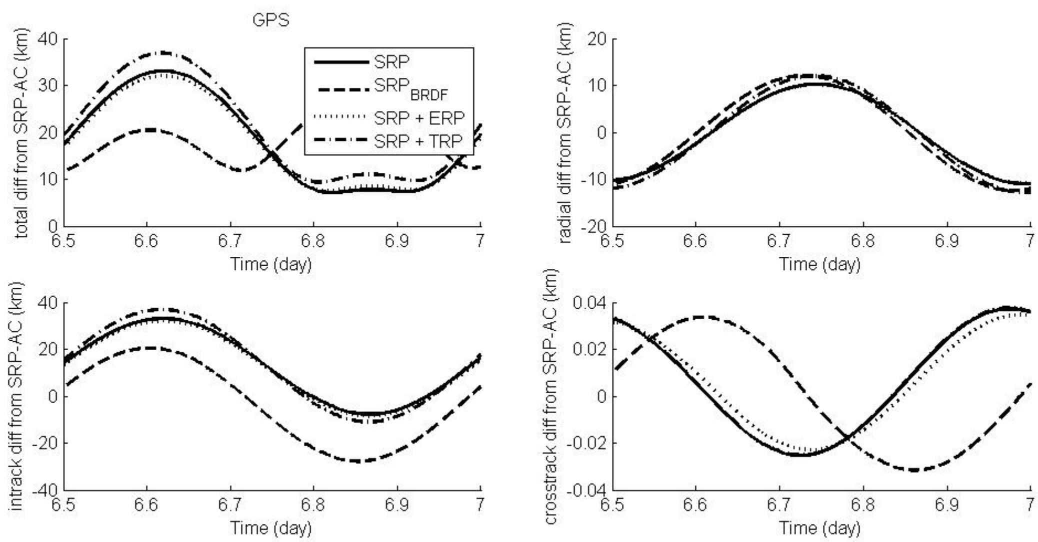

Figure 16. (a) Total Difference, (b) Radial Difference, (c) In-Track Difference, and (d) Cross-Track Difference in Positions from SRP on completely absorptive cannonball for GPS.

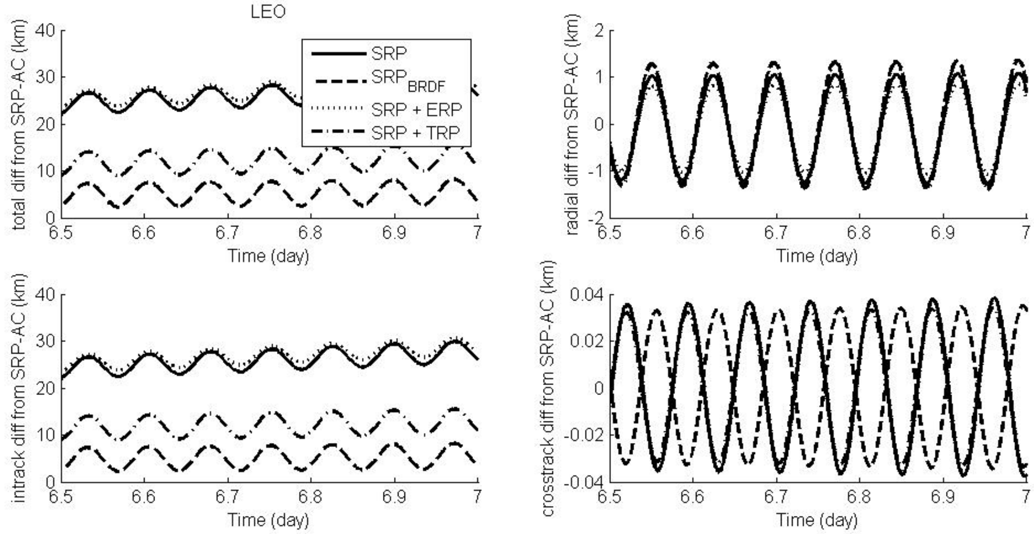

Figure 17. (a) Total Difference, (b) Radial Difference, (c) In-Track Difference, and (d) Cross-Track Difference in Positions from SRP on completely absorptive cannonball for LEO.

Figures 18-20 plot the total difference, radial difference, in-track difference, and cross-track difference for positions calculated using the BRDF-corrected SRP, SRP + ERP, and SRP + TRP as compared to the position with SRP only as a function of time for the last half day of the simulation. In this particular simulation, the BRDF correction produces the largest variation followed by the TRP and then the ERP with only minor differences. Variations in orbit, SO shape, and surface properties would undoubtedly produce different magnitudes. For high fidelity orbit propagation, all these non-gravitational forces need to be accounted.

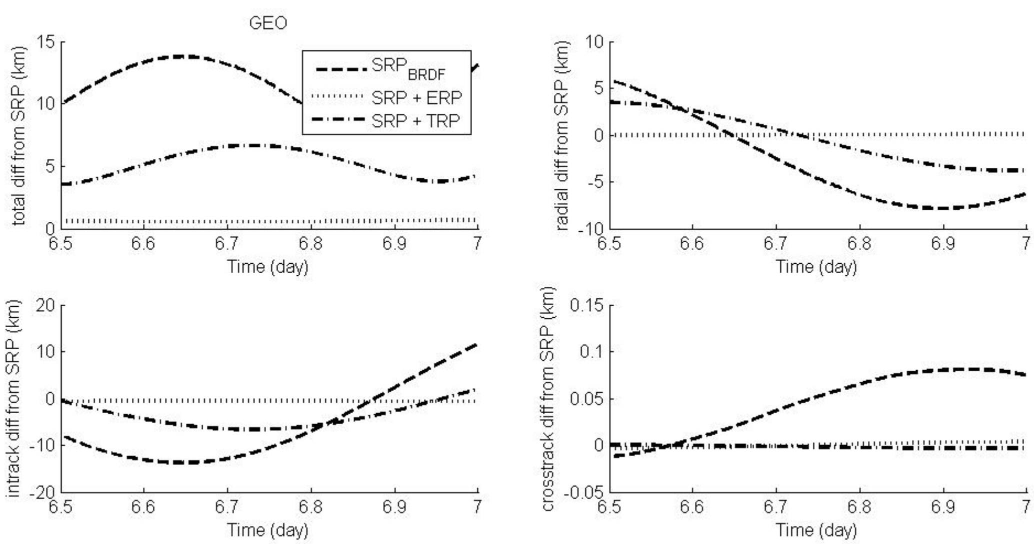

Figure 18. (a) Total Difference, (b) Radial Difference, (c) In-Track Difference, and (d) Cross-Track Difference in Positions from SRP-Only Case for GEO.

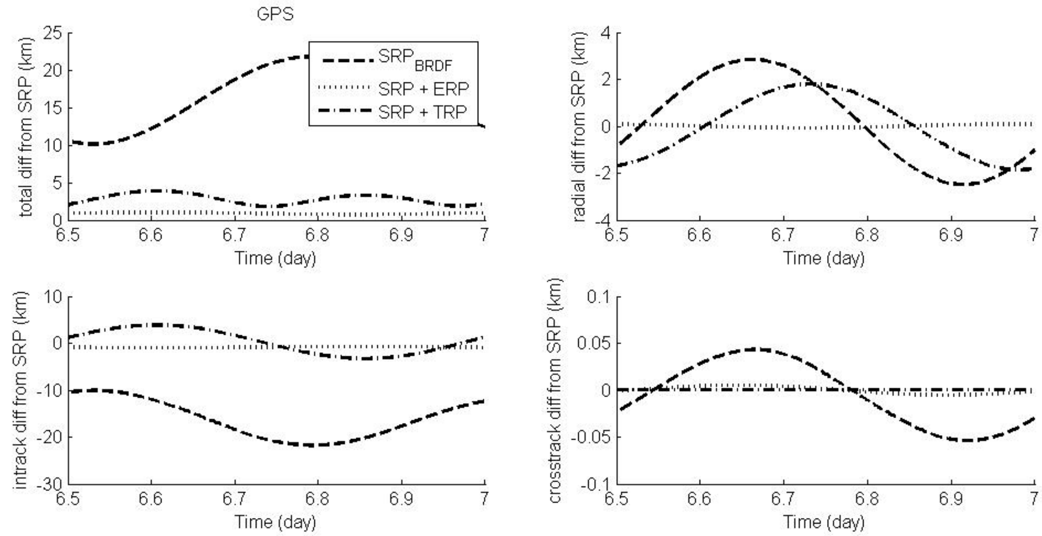

Figure 19. (a) Total Difference, (b) Radial Difference, (c) In-Track Difference, and (d) Cross-Track Difference in Positions from SRP-Only Case for GPS orbit.

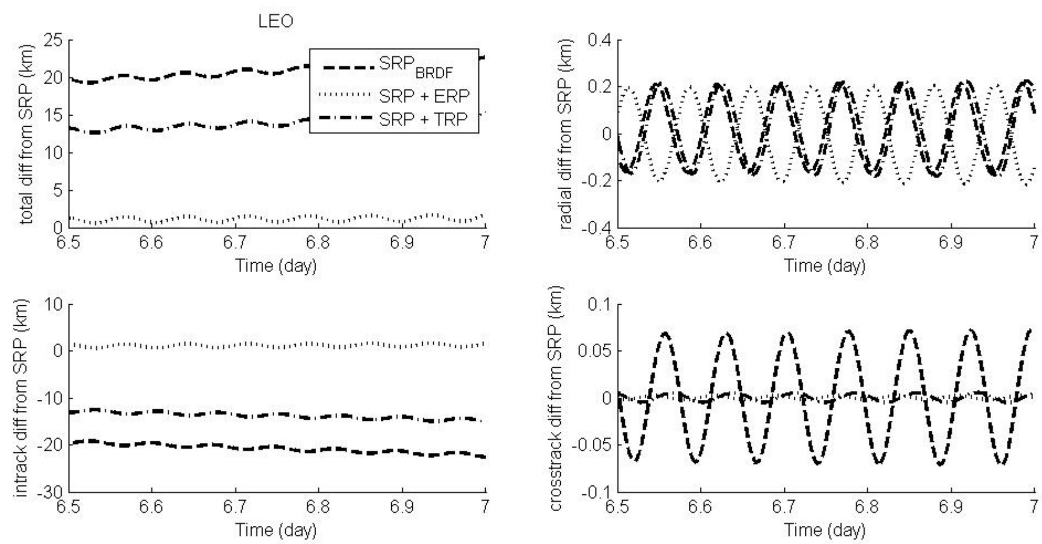

Figure 20. (a) Total Difference, (b) Radial Difference, (c) In-Track Difference, and (d) Cross-Track Difference in Positions from SRP-Only Case for LEO.

CONCLUSION

Brightness models are dependent on the surface BRDF. Current radiation pressure models, however, ignore the BRDF, even though the BRDF has a significant affect on the magnitude and direction of the resulting radiation pressures. It was shown in this paper how the models used to calculate the various radiation pressures can be made consistent with the model used to calculate the brightness of a SO. This required the addition of BRDF-specific correction factors to the calculation of the SRP and ERP, and the development of a new model for the TRP. The effect of a SO's shape and attitude on its orbital position is through the various non-gravitational forces. Making this connection more physically realistic strengthens the possibility of using simultaneous angles and brightness measurements to estimate a SO's shape and attitude. In addition, and critically, this study suggests that for space debris whose interactions with electro-magnetic radiation are described accurately with a BRDF, then hitherto unknown torques resulting from differences in the specular reflectance with illumination angle would account for rotational characteristics affecting both tracking signatures and the ability to predict the orbital evolution of the objects. In practice, the surface parameters of a particular BRDF model are first chosen to approximate a given material, whether highly specular as with aluminum or Mylar, or more diffuse as with paint. The observed light curves are then used to refine the parameters that define the surface BRDFs, and these parameters, in turn, refine the SRP calculation to improve the propagation of the orbit and spin state analysis of the SO.

ACKNOWLEDGEMENTS

This work is sponsored by a Small Business Innovative Research (SBIR) contract FA9453-11-C-0154 by the Air Force Research Laboratory (AFRL) at Kirtland Air Force Base, and contract FA8655-11-1-3043 by the European Office of Aerospace Research and Development (EOARD), London UK. The authors also wish to acknowledge useful discussions and technical contributions made by other members of the SBIR team: Daron Nishimoto, Keric Hill, Steve Lyke, Kris Hamada, and Channing Chow of Pacific Defense Solutions, LLC

REFERENCES

[1] Schildknecht, et al., "Properties of the High Area-to-mass Ratio Space Debris Population in GEO," *The Advanced Maui Optical and Space Surveillance Technologies Conference*, Wailea, Maui, HI, Sept, 2005.

[2] Kelecy, T., Payne, T., Thurston R., and Stansbery, G., "Solar Radiation Pressure Estimation and Analysis of a GEO Class of High Area-to-mass Ratio Debris Objects", AAS 07-391, *AAS Astrodynamics Specialist Conference*, Mackinac Island, MI, August 2007.

[3] Kelecy, T., Baker, E., Seitzer, P., Payne, T., and Thurston, R., "Prediction and Tracking Analysis of a Class of High Area-to-mass Ratio Debris Objects in Geosynchronous Orbit," *The Advanced Maui Optical and Space Surveillance Technologies Conference*, Wailea, Maui, HI, Sept 16-19, 2008.

[4] Kelecy, T., and Jah, M., "Analysis of Orbit Prediction Sensitivity to Thermal Emissions Acceleration Modeling for High Area-to-mass Ratio (HAMR) Objects," *The Advanced Maui Optical and Space Surveillance Technologies Conference*, Wailea, Maui, HI, Sept. 1-4, 2009

[5] Linares, R., Crassidis, J. L., Jah, M. K., and Kim, H., "Astrometric and Photometric Data Fusion for Resident Space Object Orbit, Attitude, and Shape Determination Via Multiple-Model Adaptive Estimation," *AAS/AIAA Astrodynamics Specialists Conference*, Vol. AIAA-8341, 2010.

[6] Ashikhmin, M., and Shirley, P., "An Anisotropic Phong BRDF Model," *Journal of Graphics Tools*, Vol. 5, No. 2, 2000, pp.25-32.

[7] Schlick, C., "An inexpensive BRDF model for physically-based rendering," *Computer Graphics Forum*, 13(3), 1994, pp. 233-246.

[8] Phong, B. T., "Illumination for computer generated pictures" *Communications of the ACM*, 18(6):311–317, June 1975

[9] Blinn, J. F., "Models of Light Reflection for Computer Synthesized Pictures," *Computer Graphics Proceedings, Annual Conference Series*, 1977, ACM SIGGRAPH, pp. 192-198

[10] Torrance, K. E., and Sparrow, E. M., "Theory for off-specular reflection from roughened surfaces," *Journal of the Optical Society of America*, 57(9):1105–1114, Sept. 1967

[11] Cook, R. L., and Torrance, K. E., "A reflectance model for computer graphics," *ACM Transactions on Graphics*, 1(1):7–24, Jan. 1982.

[12] Knocke, P. C., Ries, J. C., and Tapley, B. D., "Earth Radiation Pressure Effects on Satellites," *Proceedings of the AIAA/AAS Astrodynamics Conference*, August 1988, pp. 577-586.

[13] McCarthy, J. J., and Martin, T. V., "A Computer Efficient Model of Earth Albedo Satellite Effects," NASA Goddard Space Flight Center, Planetary Sciences Department Report no. 012-77, 1977

[14] Rakhmanov, E. A., Saff, E. B. and Zhou, Y. M., "Minimal Discrete Energy on the Sphere," *Math. Res. Lett*. 1, 1994, pp. 647-662.

[15] Saff, E. B., and Kuijlaars, A.B.J., "Distributing Many Points on a Sphere," *The Mathematical Intelligencer*, Vol. 19, No. 1, 1997, pp. 5-11.

[16] Marshall, J. A., and Luthke, S. B., "Modeling Radiation Forces Acting on Topex/Poseidon for Precision Orbit Determination," *Journal of Spacecraft and Rockets*, Vol. 31, No. 1, 1994, pp. 99-105.

[17] Vallado, D. A., *Fundamentals of Astrodynamics and Applications*, McGraw-Hill, New York, NY, 3rd ed., 1997, pp. 574–578.

[18] Shuster, M. D., "A Survey of Attitude Representations," *Journal of the Astronautical Sciences*, Vol. 41, No. 4, Oct.-Dec. 1993, pp. 439–517.